Electronic Supplementary Material (ESI) for Physical Chemistry Chemical Physics.

Following the Unusual Breathing Behaviour of ^{17}O-Enriched Mixed-Metal (Al,Ga)-MIL-53 using NMR Crystallography

Cameron M. Rice,[1] Zachary H. Davis,[1] David McKay,[1] Giulia P. M. Bignami,[1]
Ruxandra G. Chitac,[1] Daniel M. Dawson,[1] Russell E. Morris,*[1,2]
and Sharon E. Ashbrook[1]*

[1] *School of Chemistry, EaStCHEM and Centre of Magnetic Resonance, University of St Andrews, St Andrews KY16 9ST United Kingdom*

[2] *Department of Physical and Macromolecular Chemistry, Faculty of Sciences, Charles University, Hlavova 8, 128 43 Prague 2, Czech Republic*

Supporting Information

S1. Structure of MIL-53 materials

S2. DFT calculations and generation of structural models

S3. EDX and PXRD of as-made materials

S4. Calcination of as-made Ga-MIL-53

S5. Further NMR spectra of calcined (Al,Ga)-MIL-53

S6. Characterisation of calcined (Al,Ga)-MIL-53 prepared by hydrothermal synthesis

S7. Characterisation of hydrated (Al,Ga)-MIL-53

S8. Characterisation of dehydrated (Al,Ga)-MIL-53

S1. Structure of MIL-53 materials

Figure S1.1 shows the structure of the open pore (OP) form of Al-MIL-53, along the three crystallographic axes. An expanded view of the local structure and the μ_2 hydroxyl linkage (*i.e.*, M-O(H)-M) is shown in Figure S1.2.

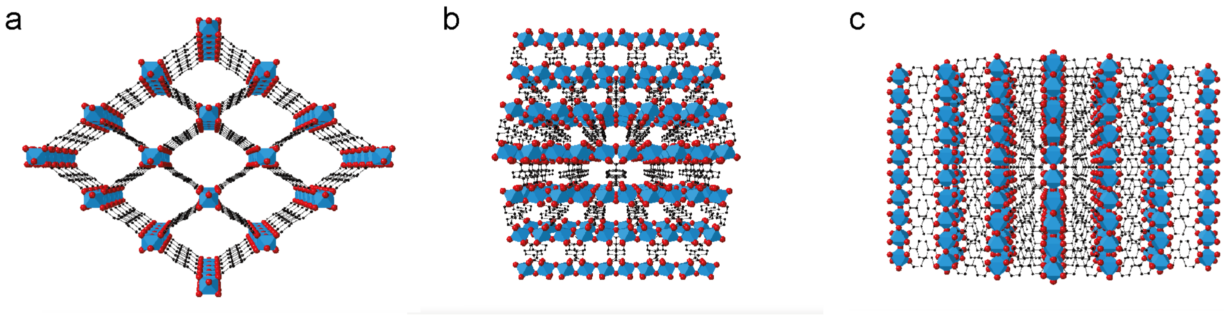

Figure S1.1. Structure of the open pore (OP) form of Al-MIL-53 along the crystallographic (a) x, (b) y and (c) z axes. Carbon and oxygen atoms are represented by black and red spheres, while the blue octahedra show the AlO_6 units. Hydrogen atoms have been omitted for clarity.

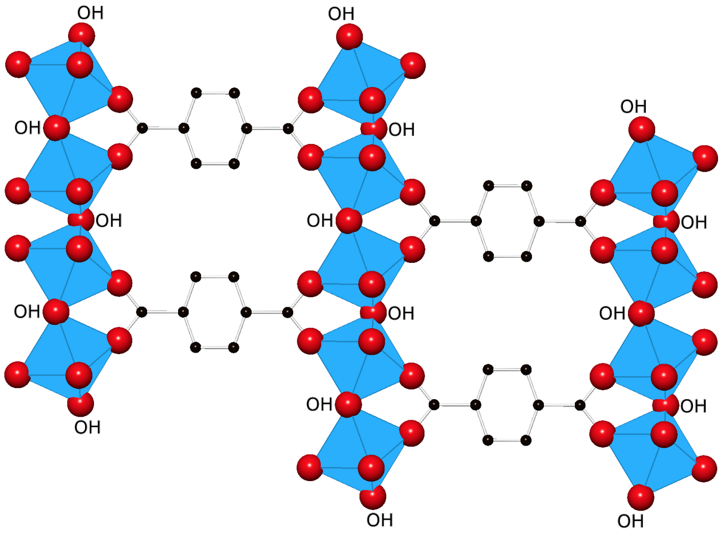

Figure S1.2. Expansion of the open pore (OP) form of Al-MIL-53, showing the local structure and the μ_2 hydroxyl linkage that links adjacent metal centres. Carbon and oxygen atoms are represented by black and red spheres, while the blue octahedra show the AlO_6 units. Hydrogen atoms have been omitted for clarity.

S2. DFT calculations and generation of structural models

Generation of initial structural models

Model structures of end-member Al-MIL-53 in OP and NP forms were generated as previously described in Ref. 22 of the main text. As such, OP structures are based on published calcined structures with H atoms added, to produce aryl and hydroxyl groups where appropriate, before optimisation with DFT (parameters as described in the Methods section of the main text). NP structures were based on the theoretical structure produced in Ref. 22, where an experimentally derived structure of hydrated Al-MIL-53 was optimised before removal of water molecules and further geometry optimisation. The Ga-containing end members were generated by swapping Al for Ga and re-optimising the geometries. To ensure compatibility of OP and NP structures and to have enough flexibility in the computed geometries for mixed-metal structures, supercells were generated such that 8 metal centres were present in the unit cell (before the geometry optimisations mentioned above). For the OP structures this involved transforming the unit cell to a 1 × 1 × 2 supercell. For the NP structures, to facilitate direct comparison with OP structures, the cell origin was translated and the cell orientation manipulated through the transformation,

$$\mathrm{T} = \begin{pmatrix} 0 & 0 & \bar{1} \\ 0 & 1 & 0 \\ 1 & 0 & 0 \end{pmatrix}, \qquad \text{(S2.1)}$$

resulting in an exchange of the a and c cell vectors. Thereafter, mixed-metal structures were generated by exchange of appropriate Al or Ga atoms to give desired composition and substitution patterns.

Ga or Al atoms were placed at the starting positions as shown in Figure S2.1, where Al-rich and Ga-rich compositions used the Al- and Ga-end-member structure, respectively, as the starting geometry. These structures allow for a range of unique substitution patterns for each chosen composition. However, it is worth noting that the use of these supercells, which have a short *x* distance, precludes the study of low doping levels along this axis, which is defined by M-OH-M chains. As a result, computed ^{27}Al NMR parameters will not include some environments (*e.g.*, Al-O-Al-O-Ga chains), see below. Table S2.1 lists all structures considered in the present study.

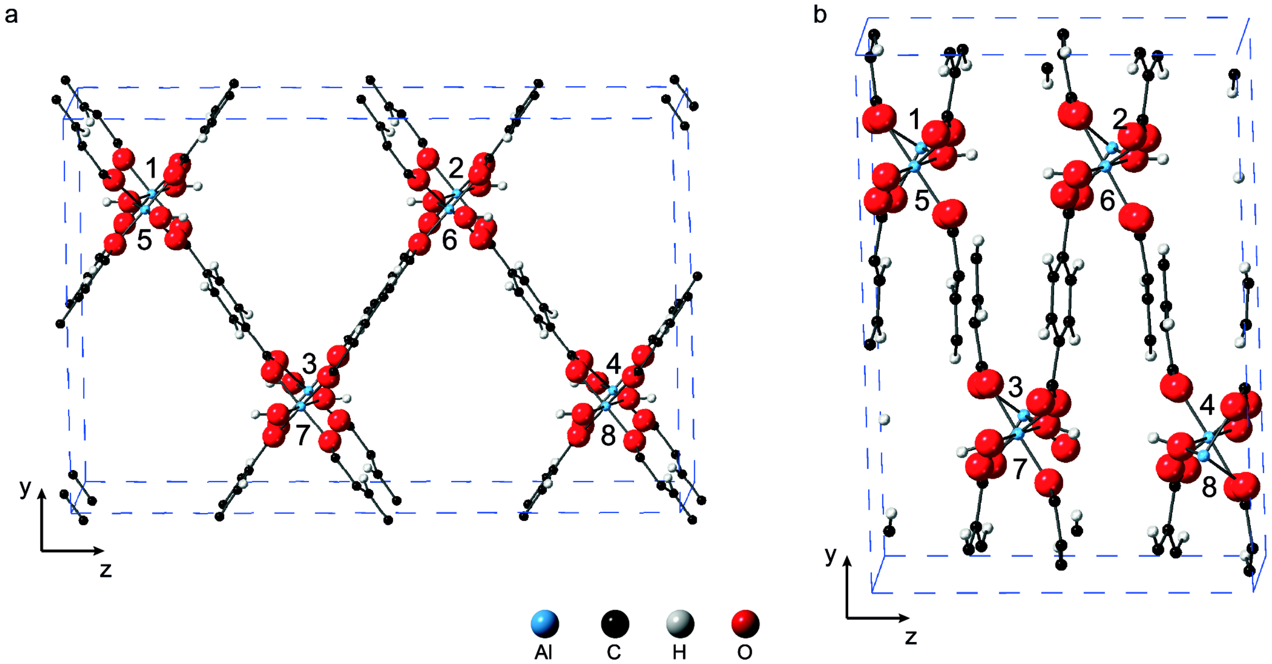

Figure S2.1. Computational (a) OP and (b) NP Al-MIL-53 structures with numbering showing positions for Ga/Al substitution to give desired compositions and substitution patterns.

Table S2.1. Compositions and substitution patterns used in the present study. Pattern numbering is directly transferable between OP and NP structures.

Pattern name	x	Parent x	Key feature[a]	Pattern name	x	Parent x	Key feature[a]
Al-MIL-53	0	0	E	Ga-1357	0.5	0	C
Ga-1	0.125	0	E	Ga-1368	0.5	0	O
Ga-12	0.25	0	L	Ga-1467	0.5	0	O
Ga-13	0.25	0	L	Ga-1678	0.5	0	L
Ga-14	0.25	0	L	Al-123	0.625	1	L
Ga-16	0.25	0	O	Al-125	0.625	1	C
Ga-17	0.25	0	O	Al-134	0.625	1	L
Ga-48	0.25	0	C	Al-135	0.625	1	C
Ga-123	0.375	0	L	Al-136	0.625	1	O
Ga-125	0.375	0	C	Al-278	0.625	1	O
Ga-134	0.375	0	L	Al-12	0.75	1	L
Ga-136	0.375	0	O	Al-13	0.75	1	L
Ga-278	0.375	0	O	Al-14	0.75	1	L
Ga-1234	0.5	0	L	Al-16	0.75	1	O
Ga-1247	0.5	0	L	Al-17	0.75	1	O
Ga-1256	0.5	0	C	Al-18	0.75	1	C
Ga-1278	0.5	0	O	Al-1	0.75	1	E
Ga-1346	0.5	0	L	Ga-MIL-53	0.75	1	E

[a] L = layers, C = chains, E = end member/low mixing and O = less ordering.

Referencing

Referencing parameters were calculated for all nuclei (^{1}H, ^{13}C, ^{17}O and ^{27}Al) by comparison of experimental and computed NMR parameters for calcined, dehydrated OP Al-MIL-53. The isotropic shielding, σ_{iso}, can be obtained from the symmetric part of the computed absolute shielding tensor, $\boldsymbol{\sigma}$, by $\sigma_{iso} = (1/3)\ \mathrm{Tr}\{\boldsymbol{\sigma}\}$. A plot of calculated σ_{iso} against experimental shifts, δ_{iso}, gives a straight line with reference shielding, $\boldsymbol{\sigma}_{ref}$, equal to the intercept where the slope is −1 or, when the slope is not equal to −1,

$$\delta_{iso} = \frac{c - \sigma_{iso}}{m}, \tag{S2.2}$$

where c and m are the intercept and slope respectively, and δ_{iso} is the computed isotropic chemical shift. Using this process for ^{1}H, ^{13}C and ^{17}O resulted in c and m values of 30.769 and −1.1172, respectively, for ^{1}H; 162.9 and −0.9498, respectively, for ^{13}C and 274.27 and −1.1001, respectively, for ^{17}O. For ^{27}Al, since just a single peak is resolved in the experiment with δ_{iso} = 3 ppm, an average of the eight ^{27}Al σ_{iso} in the computed supercell was used to calculate the reference shielding value of 556.42 ppm.

In addition, for ^{17}O, the position of the centre-of-gravity (δ_1, δ_2) in a triple-quantum MAS spectrum was calculated using the computed NMR parameters. Following the convention used in Ref. 56 of the main text, for nuclei with spin quantum number I = 5/2, δ_1 and δ_2 (quoted in in ppm) are given by

$$\delta_1 = \frac{17}{31}\delta_{iso} + \frac{32}{93}\delta_Q \ , \tag{S2.3}$$

$$\delta_2 = \delta_{iso} - \frac{16}{15}\delta_Q \ , \tag{S2.4}$$

where

$$\delta_Q = \left(\frac{3000}{40}\frac{P_Q}{\nu_0}\right)^2 \ , \tag{S2.5}$$

with ν_0 = 81.4 MHz and 115.25 MHz for experiments at B_0 = 14.1 T and 20.0 T, respectively, and

$$P_Q = C_Q\sqrt{(1 + \frac{\eta_Q^2}{3})} \ . \tag{S2.6}$$

Results

Figure S2.2 shows the energy differences between OP and NP structures of mixed-metal $(Al_{1-x}Ga_x)$-MIL-53, for a given composition and substitution pattern. With dispersion corrections included (PBE-TS), the OP structures are consistently 5.5 to 6.0 eV higher in energy than NP structures. Conversely, when dispersion corrections are not included (PBE), OP structures are consistently 3.0 to 4.0 eV *lower* in energy than their NP counterparts. This suggests, therefore, that the choice of whether or not to use a dispersion correction (and indeed the accuracy of the scheme chosen) can affect which structure is more stable.

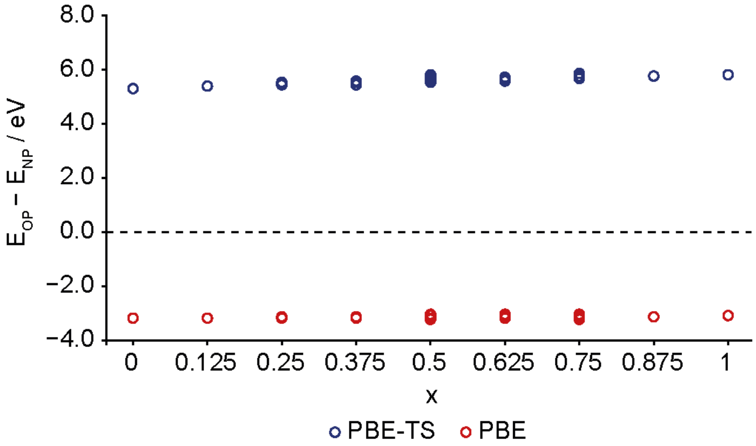

Figure S2.2. Energy difference between the OP and NP form of mixed-metal $(Al_{1-x}Ga_x)$-MIL-53, plotted as a function of composition, for DFT calculations carried out with (blue) and without (red) the inclusion of dispersion corrections.

In order to investigate this difference further, the value of the dispersion correction at each composition was plotted for NP and OP structures separately in Figure S2.3. In the NP form, the correction is consistently large, at −10.7 to −11.1 eV, and there is no trend with composition. This suggests the dispersion correction is dictated by the proximity of the BDC linkers in the NP form. Conversely in the OP form, the dispersion correction is smaller, from −2.0 to −2.3 eV and shows a strong dependence on composition. This is also mirrored in the trends in supercell volume with composition, as shown in Figure S2.4. This suggests that the dispersion correction in the OP form is dictated by the overall pore size. The true energy difference between compositionally analogous OP and NP forms is therefore difficult to ascertain, with different factors affecting the two forms and the magnitude of dispersion energy they exhibit. It is known from previous studies on MIL-53 (see Refs. 46 and 67 of the main text) that the inclusion of a dispersion correction is necessary to obtain the correct structure for this flexible MOF.

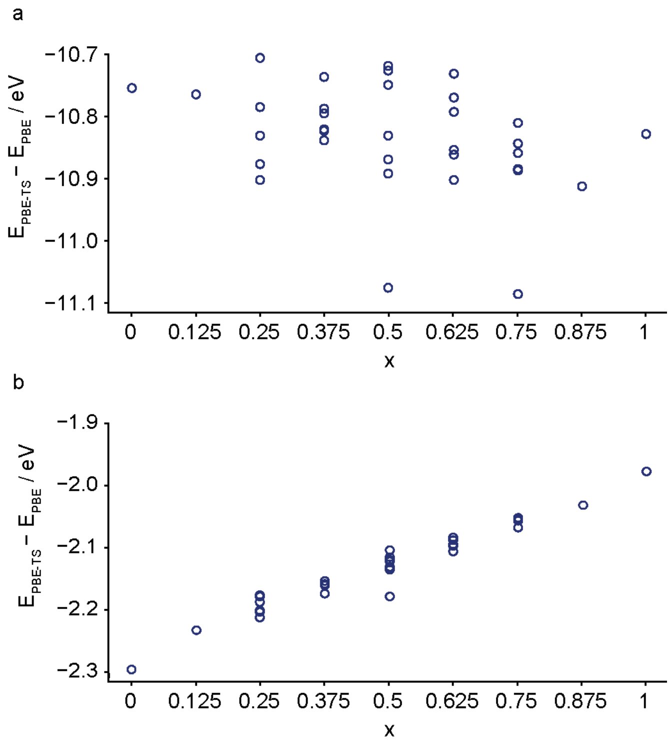

Figure S2.3. Energy difference upon the inclusion of dispersion corrections in the DFT calculations for (a) NP and (b) OP forms of mixed-metal ($Al_{1-x}Ga_x$)-MIL-53, plotted as a function of composition.

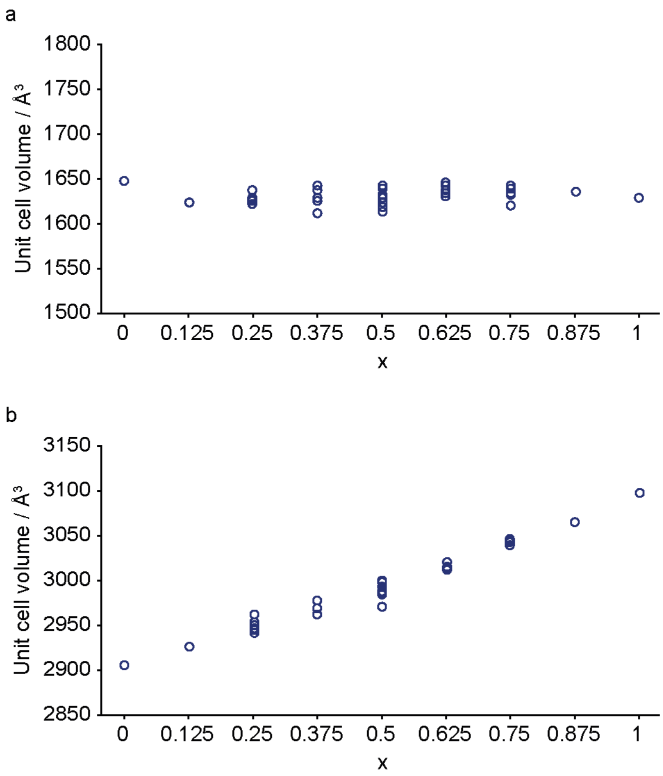

Figure S2.4. Variation in unit cell volume, as calculated by DFT, of (a) NP and (b) OP forms of mixed-metal ($Al_{1-x}Ga_x$)-MIL-53, as a function of composition.

Figure S2.5 shows mixing enthalpies, E_{mix}, of the OP MOFs, analogous to Figure 7b of the main text, which shows E_{mix} for NP forms. E_{mix} is given by

$$E_{mix} = E(x_i) - ((x_1 - x_i)\,E(x_0) + x_i\,E(x_1))\ , \tag{S2.7}$$

where $x_0 = 0$ and $x_1 = 1$ (see Table S2.1). For the OP case, there is considerable overlap between the different types of cation arrangements considered. However, it does appear that models with less ordering are perhaps favoured at compositions around $x = 0.5$, and that layers of similar cations are typically preferred to chains.

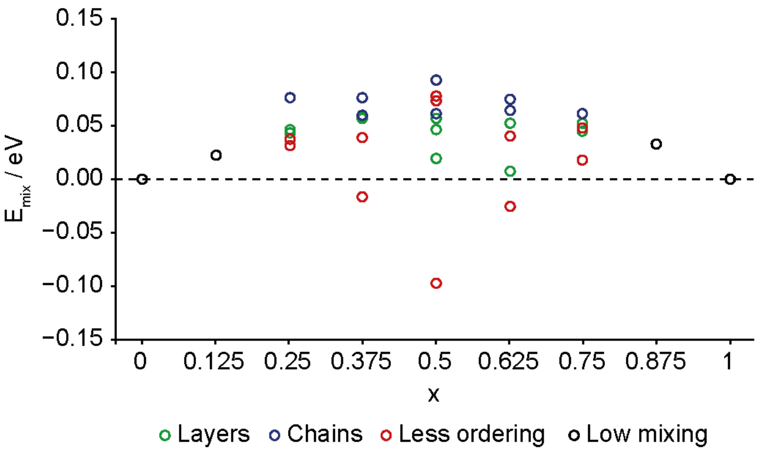

Figure S2.5. Variation in calculated mixing energy of OP mixed-metal ($Al_{1-x}Ga_x$)-MIL-53 as a function of composition. The colours denote different types of spatial arrangements of the cations.

Figure S2.6 plots the predicted centre-of-gravity (δ_1, δ_2) of a resonance in a (sheared) triple-quantum MAS spectrum (at B_0 = 14.1 T and 20.0 T) for ^{17}O species present in the structural models, given the parameters computed herein.

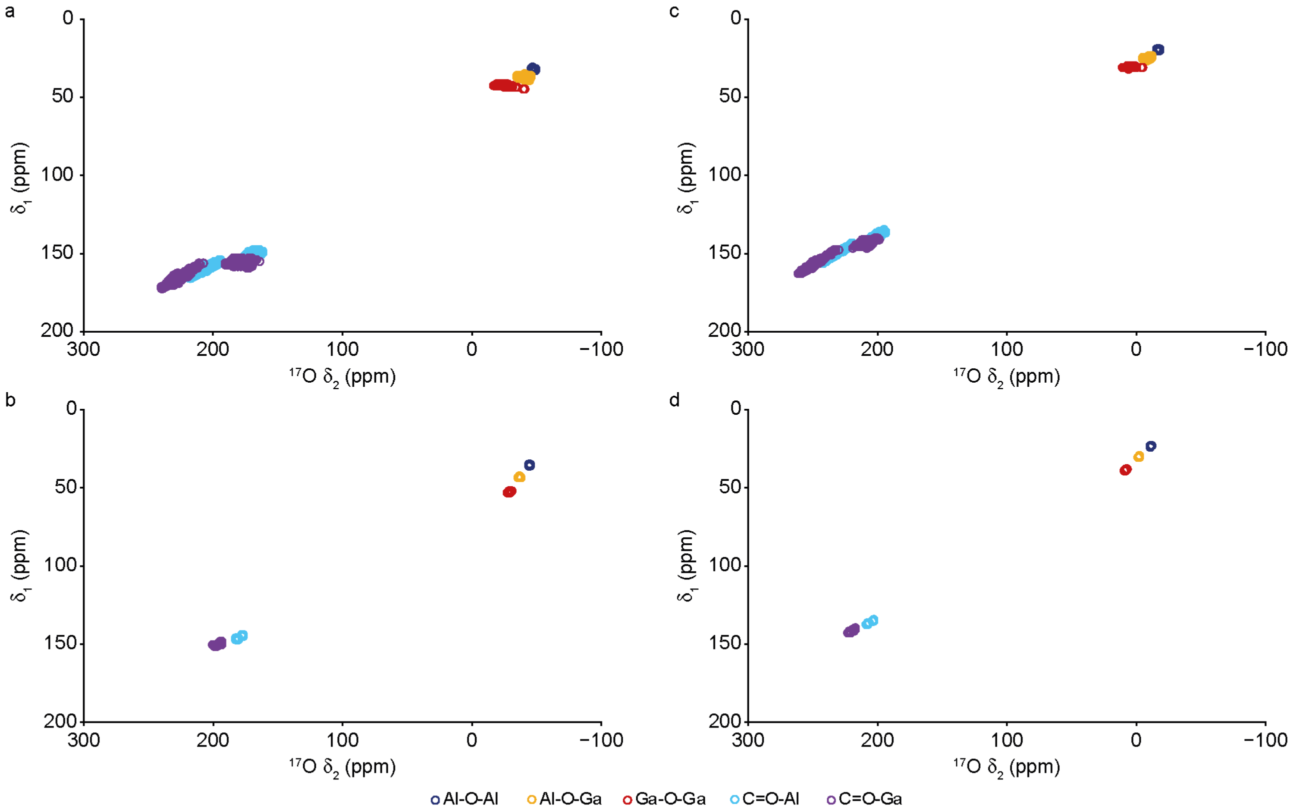

Figure S2.6. Calculated ^{17}O δ_1 and δ_2 positions of the centre of gravity of a resonance in an MQMAS spectrum (after shearing) with (a, b) B_0 = 14.1 T and (c, d) 20.0 T, for (a, c) NP and (b, d) OP forms of mixed-metal ($Al_{1-x}Ga_x$)-MIL-53.

Computed ^{1}H chemical shifts (Figure S2.7) are found to change little across the compositional series. The ^{1}H chemical shifts for the OP form of Al/Ga-MIL-53 (Figure S2.7b) shows hydroxyl species at 2-4 ppm that are reasonably well separated by coordination to two Al centres, two Ga centres or one Al and one Ga. Aryl ^{1}H species exhibit a narrow range of shifts around ~8 ppm. In the NP form (Figure S2.7a), ranges in shift are larger across series due to the reduction in symmetry. This is most apparent in the aryl ^{1}H shifts, owing to the loss of equivalency between these species through rotation along the M-BDC-M axes. In general, ^{1}H shifts are lower than the corresponding values predicted for the OP form. In the case of the aryl ^{1}H species, the extent of deshielding may be enough to separate OP and NP resonances by ^{1}H MAS (assuming a sufficiently fast MAS rate and/or homonuclear decoupling were available to average the dipolar coupling). However, the OH protons of OP and NP forms are likely to show significant overlap.

Figure S2.8 plots computed ^{27}Al δ_{iso} against composition for NP and OP forms of the mixed-metal MIL-53 materials, while Figure S2.9 plots computed ^{27}Al C_Q against δ_{iso}. For both forms, a distribution of both quadrupolar and shielding interactions are predicted, and for each type of Al an increase in C_Q is usually accompanied by a higher δ_{iso}. In general, the NP materials have lower δ_{iso} and larger ranges of C_Q for each species. There is an apparent distinction between Al species with different connectivities through the metal-hydroxide chains (*i.e.*, those in Al-O-**Al**-O-Al and Ga-O-**Al**-O-Ga linkages), particularly in the OP form. However, resonances in experimental spectra will also be broadened by the second-order quadrupolar interaction, limiting resolution. Furthermore, the short x distance in the structural models precludes lower order mixing in that dimension, and experimental resolution is likely to be further compromised by the additional presence of Al-O-**Al**-O-Ga sites, which do not occur in the current set of models.

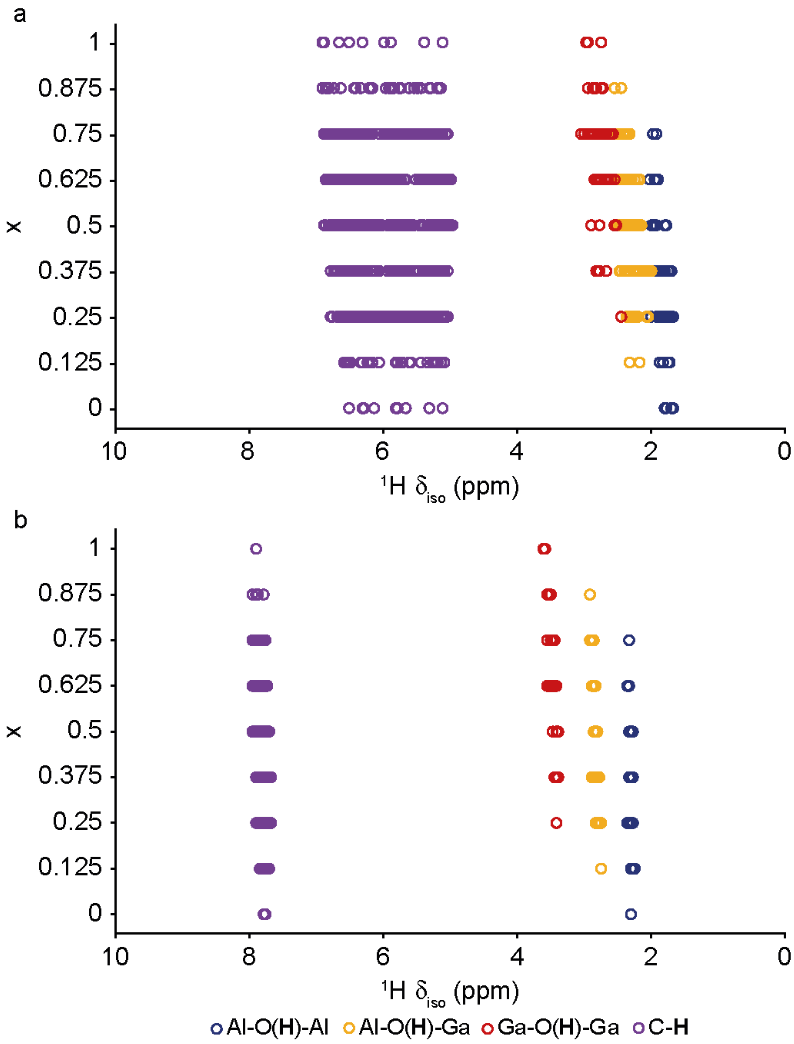

Figure S2.7. Calculated ^{1}H δ_{iso} for (a) NP and (b) OP forms of mixed-metal (Al$_{1-x}$Ga$_x$)-MIL-53.

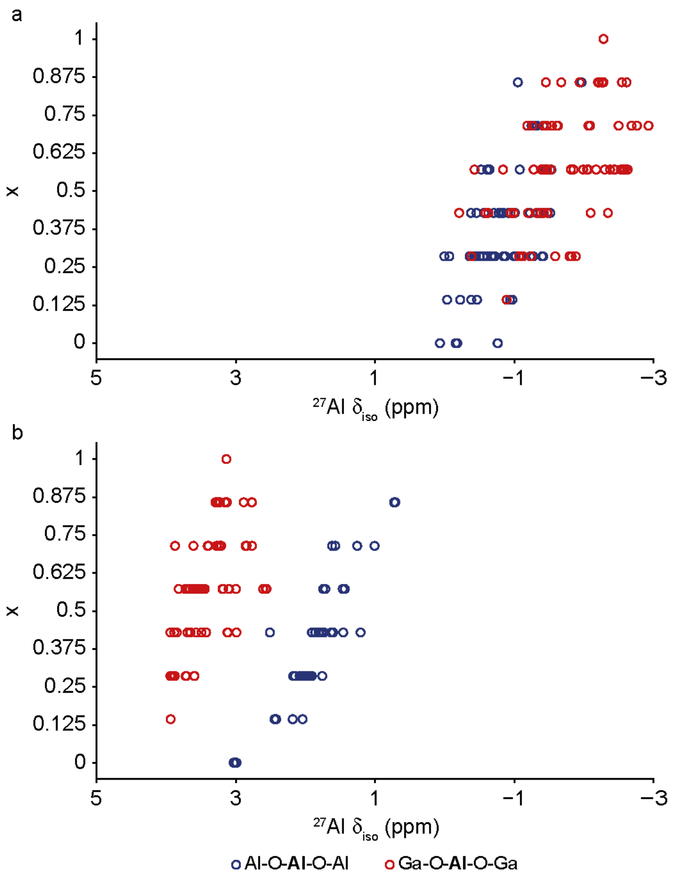

Figure S2.8. Calculated ^{27}Al δ_{iso} for (a) NP and (b) OP forms of mixed-metal ($Al_{1-x}Ga_x$)-MIL-53.

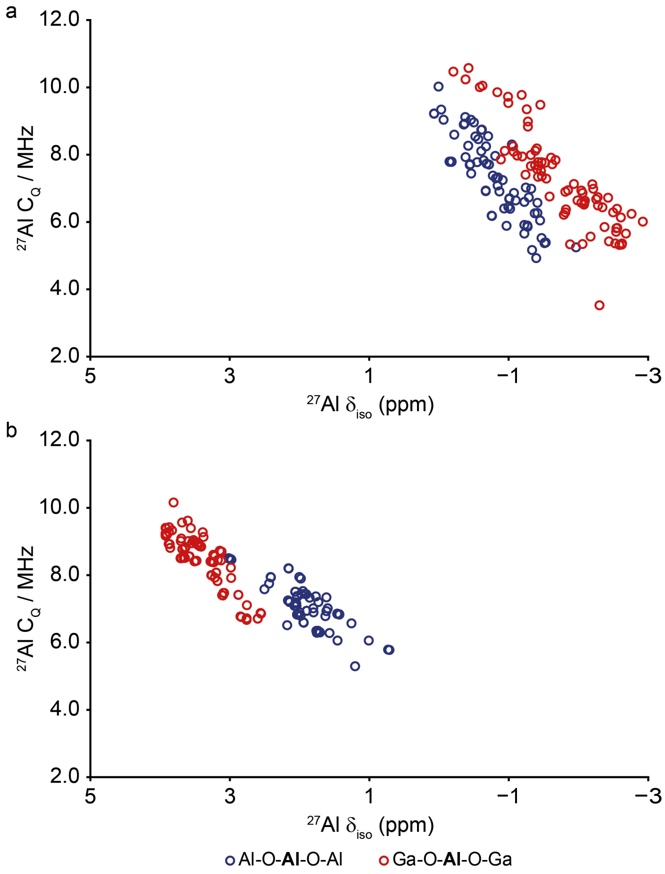

Figure S2.9. Calculated ^{27}Al NMR parameters (δ_{iso} and C_Q) for (a) NP and (b) OP forms of mixed-metal ($Al_{1-x}Ga_x$)-MIL-53.

Figure S2.10 shows the distances from the O1 hydroxyl group to the carboxylate oxygen sites in OP and CP Al-MIL-53. In the NP form, two distinct carboxylate oxygens (O2 and O3) have two different distances to the O1 hydroxyl group.

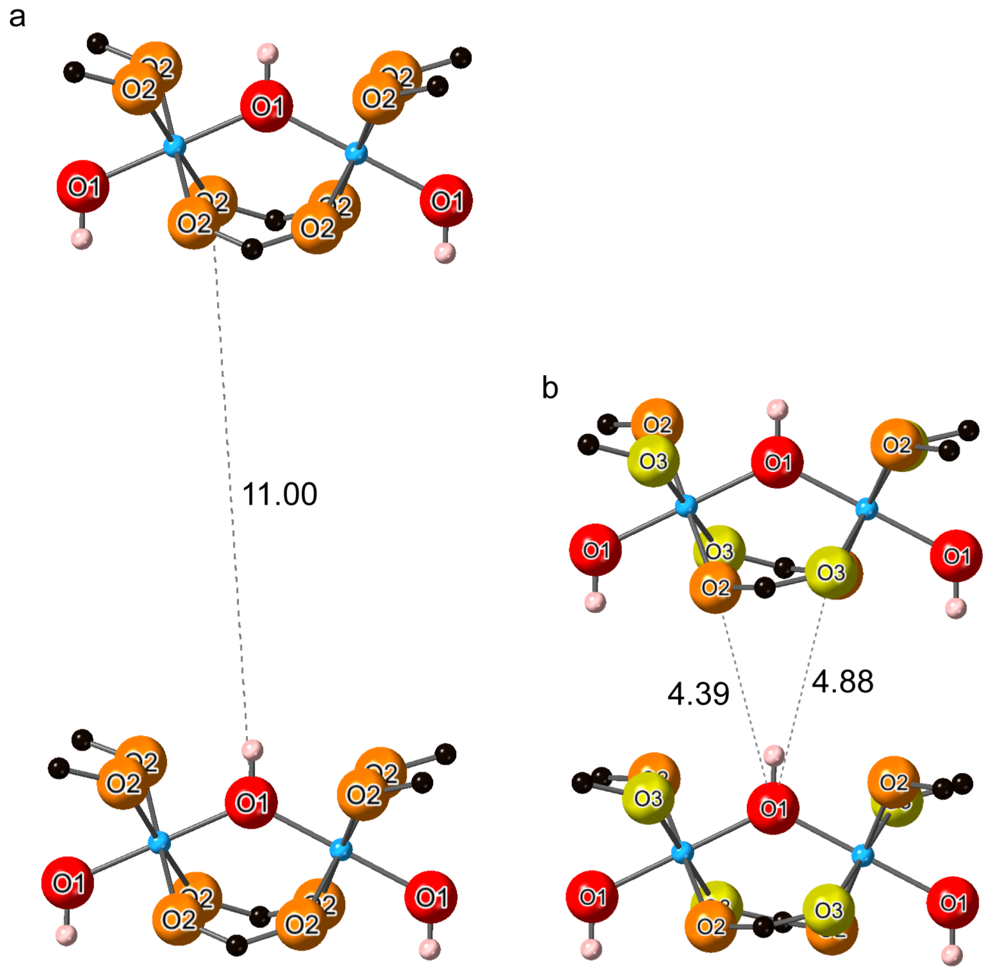

Figure S2.10. Comparative view of oxygen sites in (a) OP and (b) NP Al-MIL-53 showing O1 hydroxyl in red and carboxylate O2 and O3 (NP only) sites in orange and yellow respectively. BDC linkers (at the carboxylate C site) and M(OH) chains are truncated for clarity. O1···O2 and O1···O3 distances across the pore are given in Å.

S3. EDX and PXRD of as-made materials

Figure S3.1 shows the composition of crystallites determined by EDX for calcined, hydrated ($Al_{1-x}Ga_x$)-MIL-53 for nominal compositions of x = 0.2, 0.5, 0.8, 0.9 and 0.95. Average compositions are given in Table 2 of the main text. Although both Al and Ga are incorporated into all of the crystallites analysed, the level of Ga seen in the final product is much lower than the stoichiometry of the starting reagents, or 'nominal' composition. Some variation in composition is seen between crystallites, with standard deviations of 10.6%, 10.2%, 11.2%, 12.2% and 7.2% for x = 0.2, 0.5, 0.8, 0.9 and 0.95 respectively.

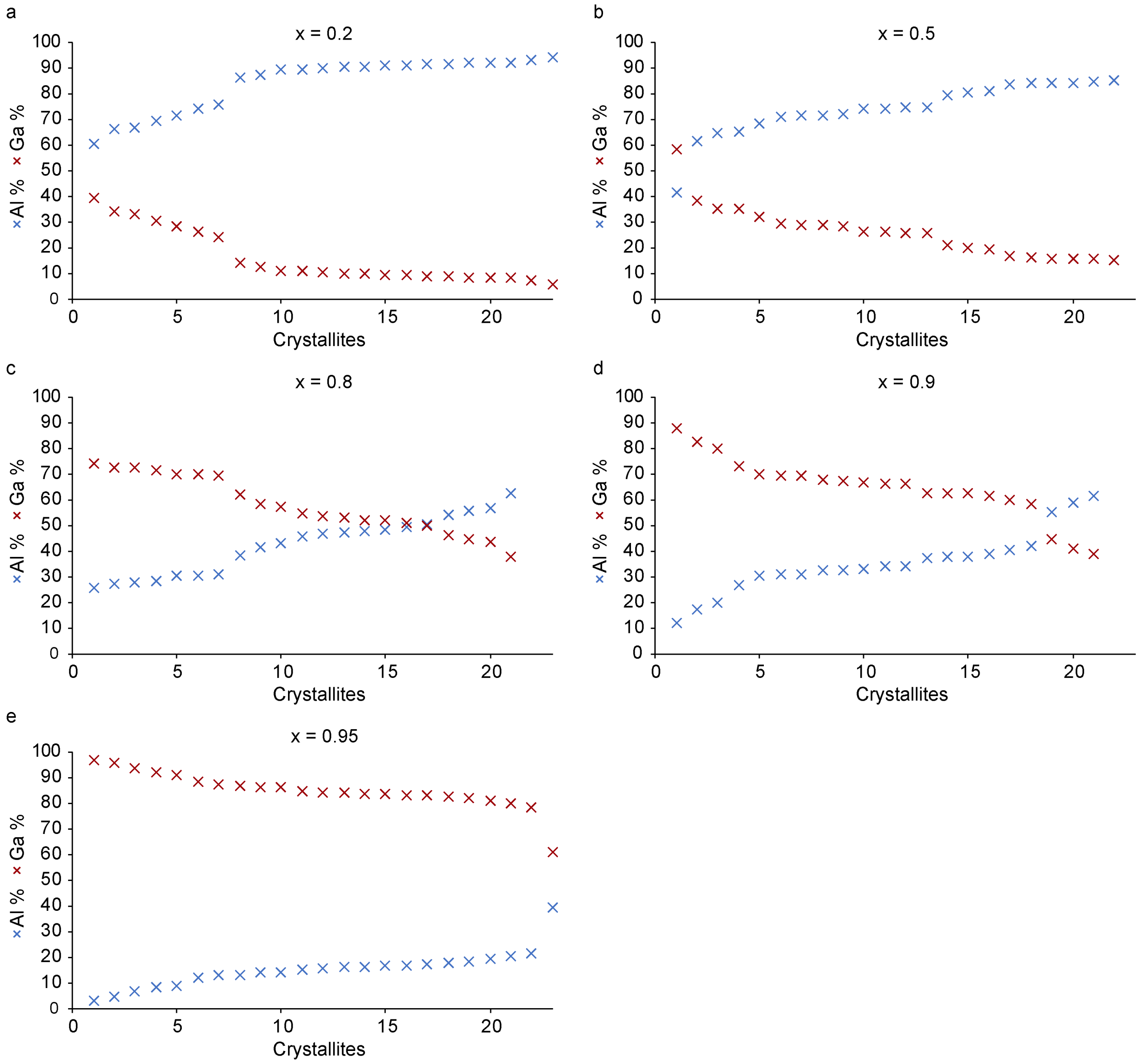

Figure S3.1. Compositions determined by EDX for calcined, hydrated ($Al_{1-x}Ga_x$)-MIL-53 for nominal compositions of x = 0.2, 0.5, 0.8, 0.9 and 0.95.

Full PXRD patterns for as-made (Al,Ga)-MIL-53 materials are shown in Figure S3.2 and a typical fit is shown in Figure S3.3. Diffraction patterns for all as-made materials confirm the successful formation of MIL-53, and are consistent with the *Pnma* space group exhibited by the end members. Broadening of the peaks is observed, likely reflecting both the variation in composition between crystallites and changes in pore size and shape as the composition varies.

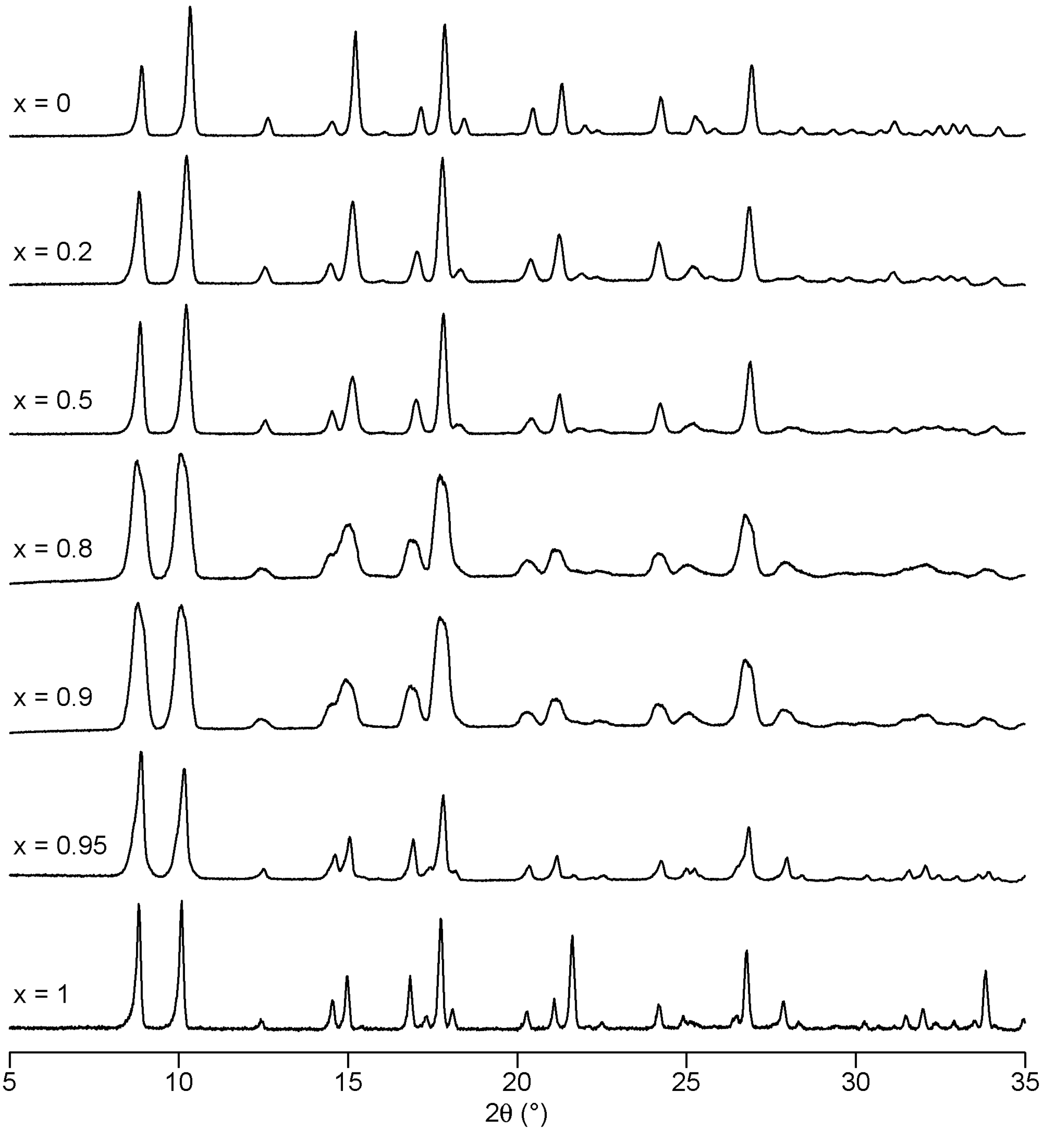

Figure S3.2. PXRD patterns of as-made ($Al_{1-x}Ga_x$)-MIL-53 for nominal compositions of x = 0, 0.2, 0.5, 0.8, 0.9, 0.95 and 1.

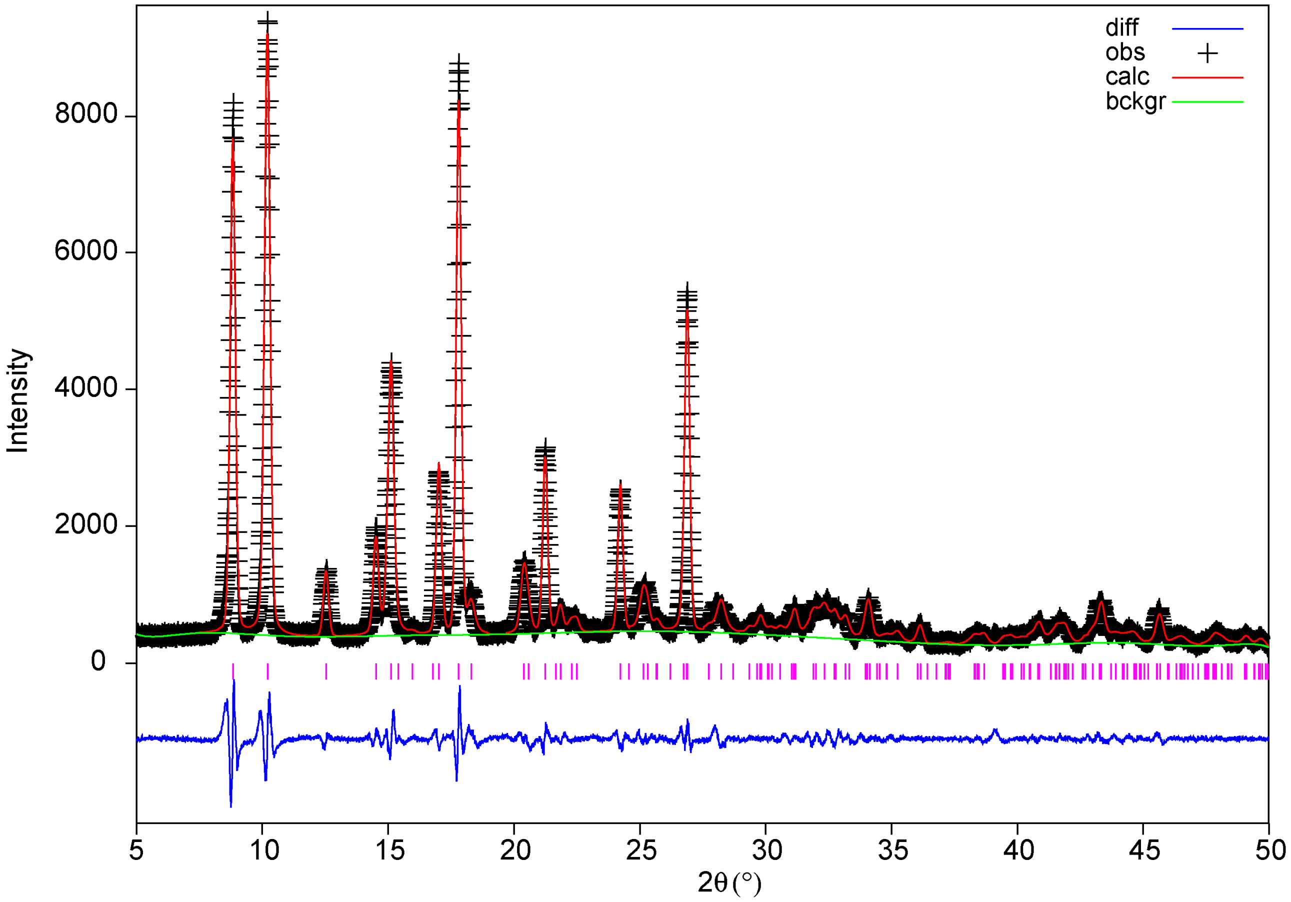

Figure S3.3. Structureless Le Bail fit of the PXRD pattern for as-made ($(Al_{1-x}Ga_x)$)-MIL-53 with a nominal composition of x = 0.5.

Corresponding patterns for calcined, rehydrated and subsequently dehydrated MOFs are shown in Figures S3.4-3.6.

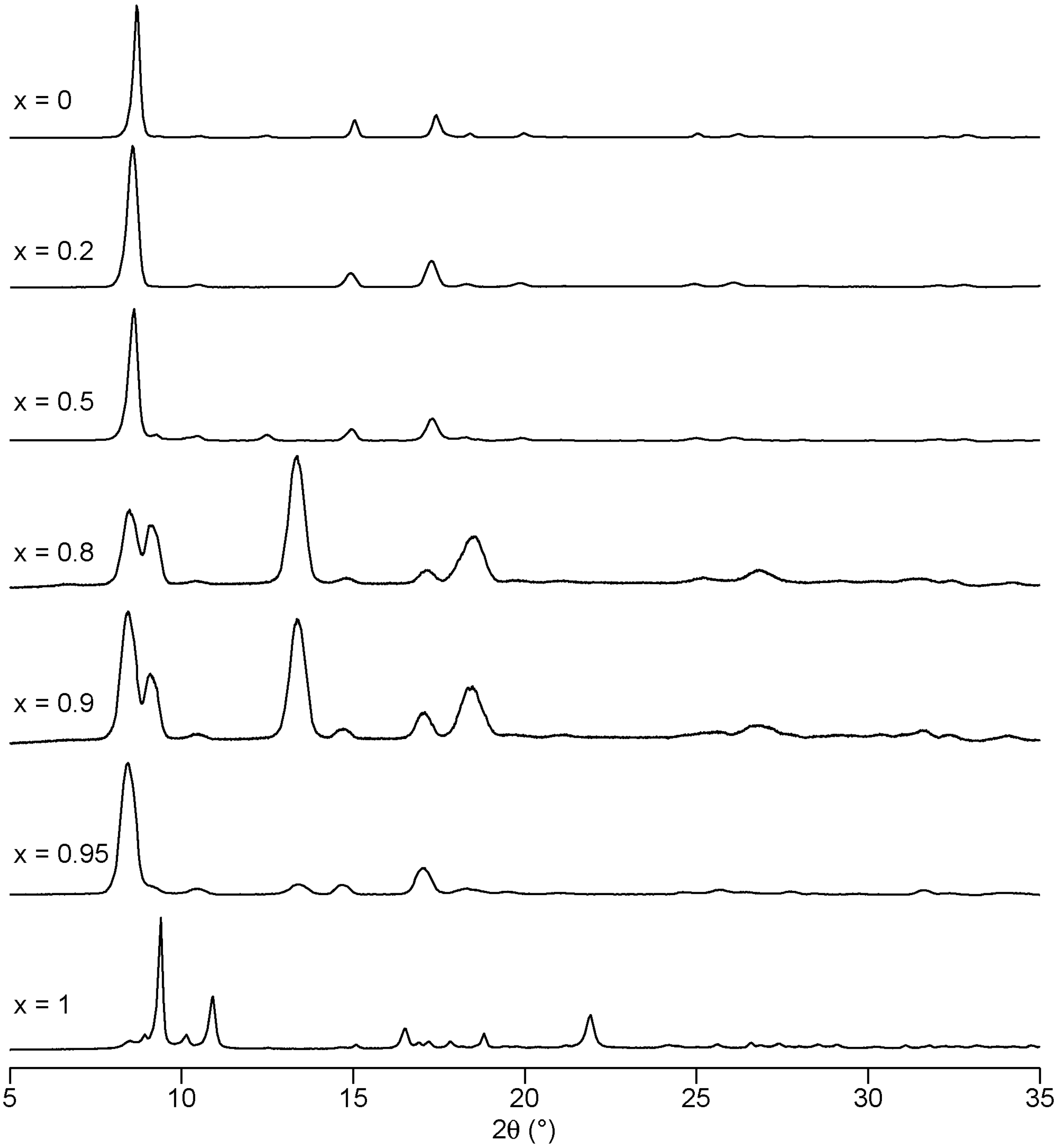

Figure S3.4. PXRD patterns of calcined ($(Al_{1-x}Ga_x)$)-MIL-53 for nominal compositions of x = 0, 0.2, 0.5, 0.8, 0.9, 0.95 and 1. (Note the lower calcination temperature for x = 1, as discussed in the main text).

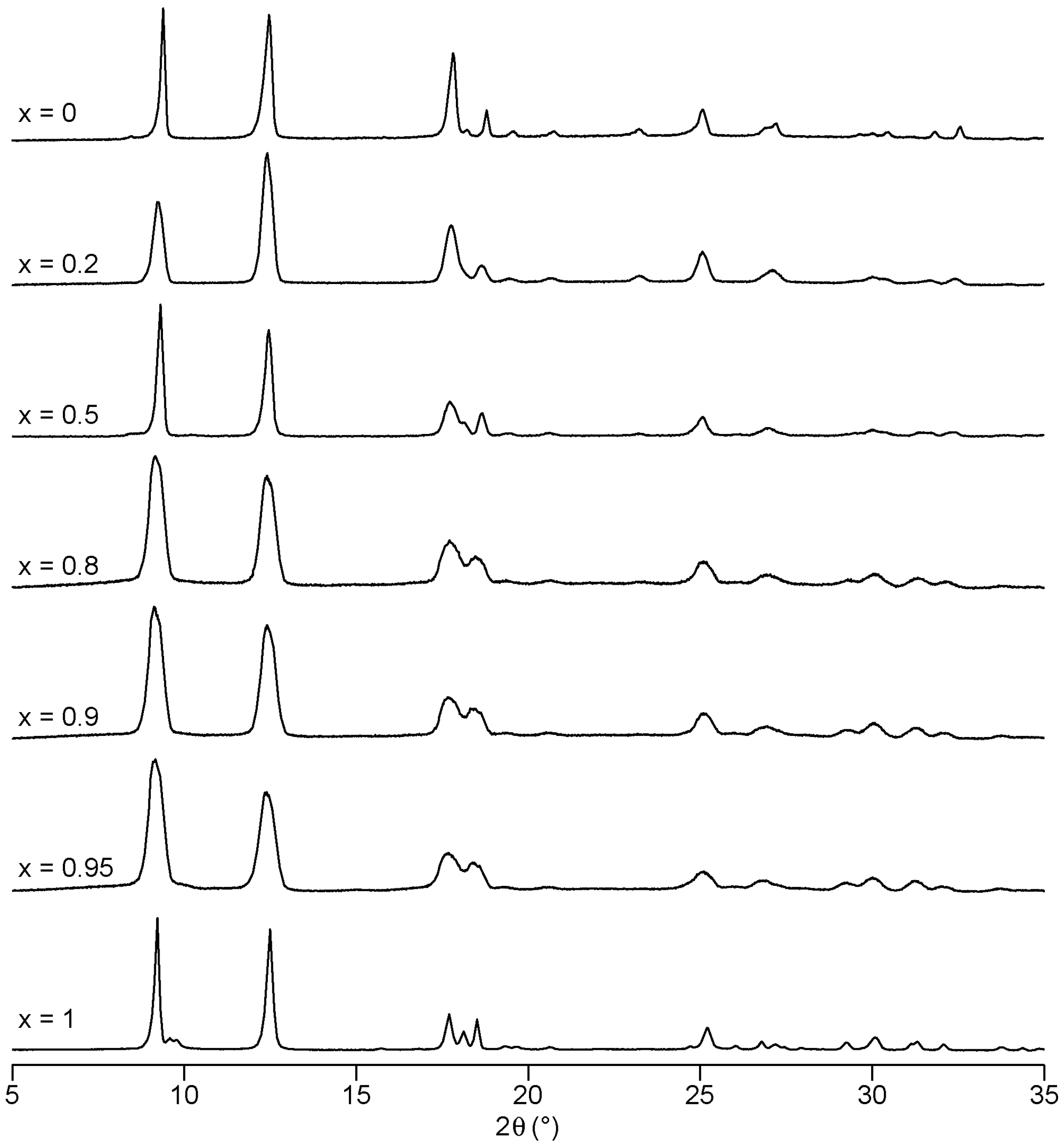

Figure S3.5. PXRD patterns of calcined, hydrated ($Al_{1-x}Ga_x$)-MIL-53 for nominal compositions of x = 0, 0.2, 0.5, 0.8, 0.9, 0.95 and 1.

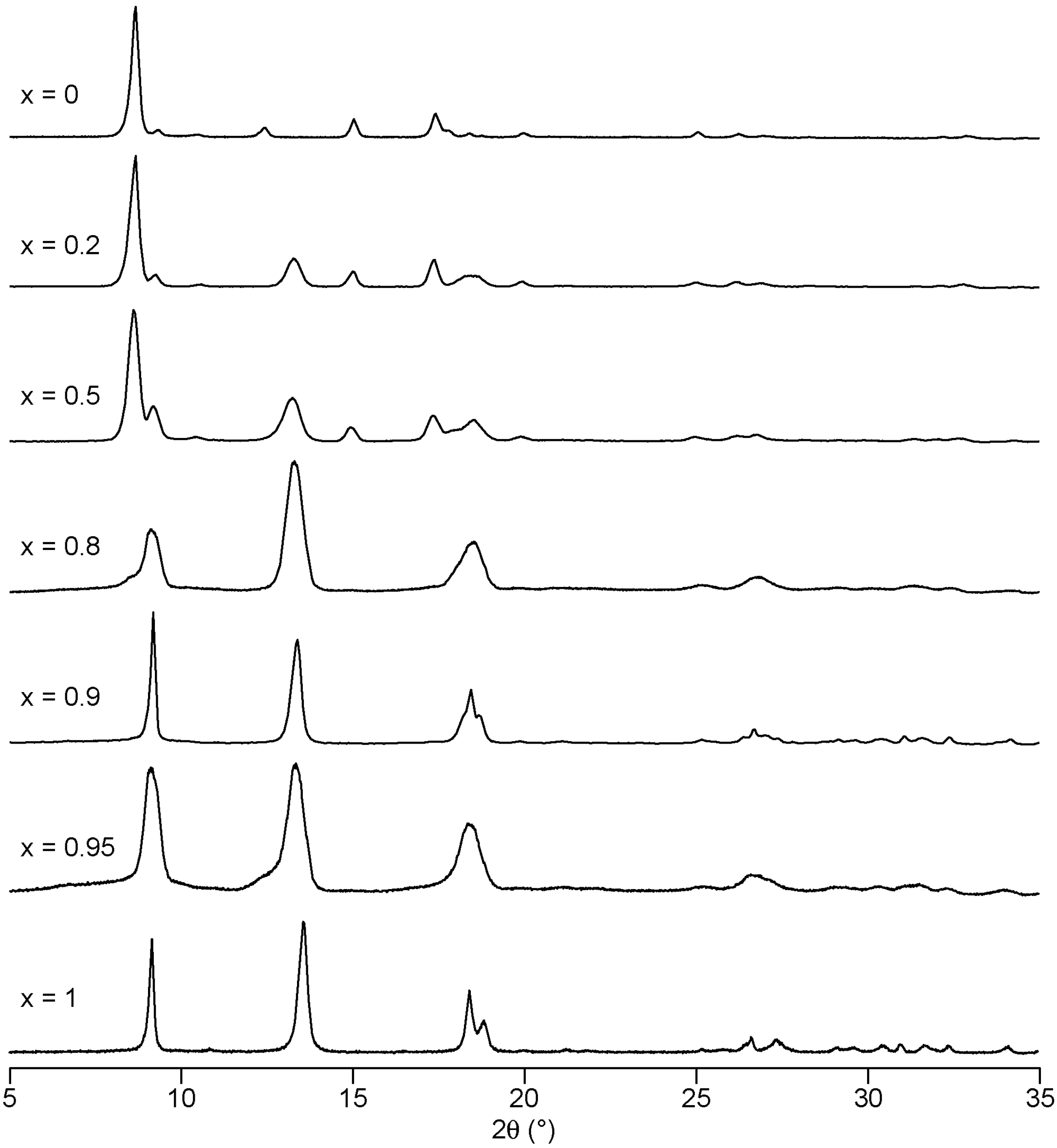

Figure S3.6. PXRD patterns of calcined, hydrated and subsequently dehydrated $(Al_{1-x}Ga_x)$-MIL-53 for nominal compositions of x = 0, 0.2, 0.5, 0.8, 0.9, 0.95 and 1.

S4. Calcination of as-made Ga-MIL-53

Figure S4.1 shows ^{13}C CP MAS NMR spectra of Ga-MIL-53 calcined at temperatures between 250 °C and 300 °C. Calcination at 250 °C produces the NP form of MIL-53, as shown by the peak at δ = 171 ppm in Figure S4.1a, whereas increasing the temperature to 260 °C results in the observation of NP and OP forms. Calcination at higher temperatures results in partial (275 °C) or complete (300 °C) decomposition. However, as shown in Figure S4.2, the relative proportion of NP and OP forms obtained varies when repeating the reaction at identical conditions (*e.g.*, compare Figures S4.1b and S4.2a), and with the time taken between calcination and spectral acquisition (Figure S4.2).

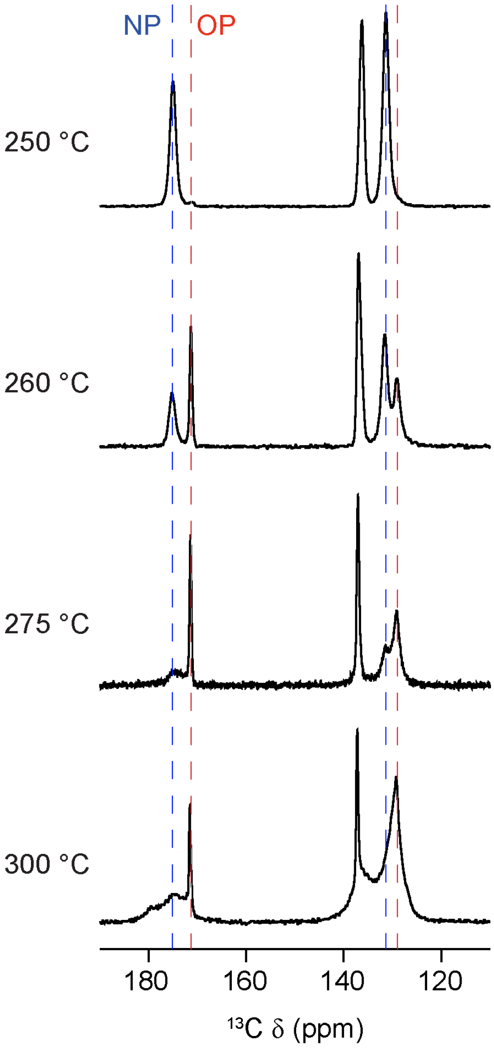

Figure S4.1. ^{13}C (14.1 T, 12.5 kHz) MAS NMR spectra of Ga-MIL-53 calcined for 96 h at (a) 250 °C, (b) 260 °C, (c) 275 °C and (d) 72 h at 300 °C.

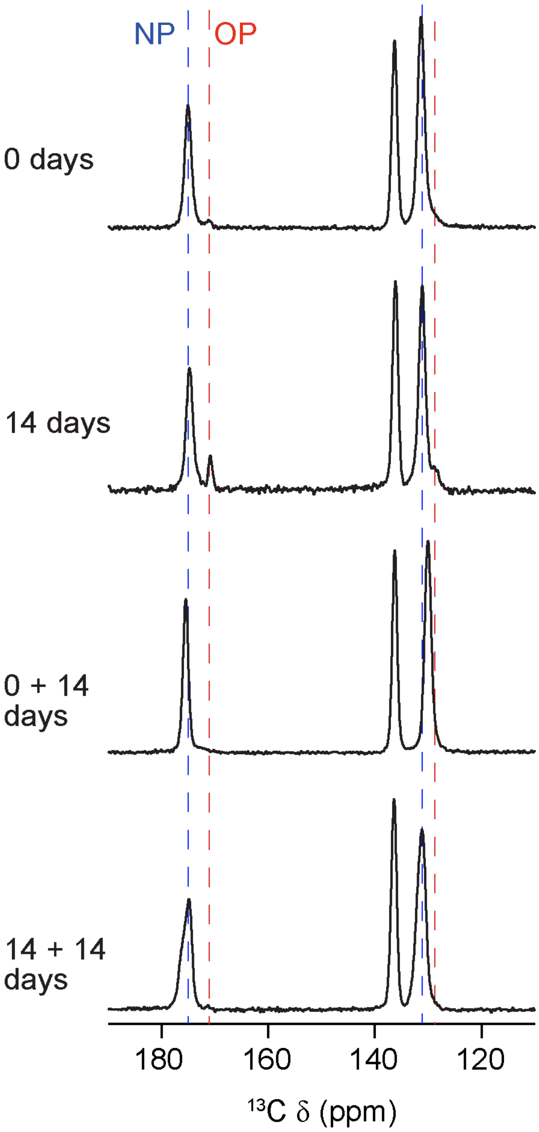

Figure S4.2. ^{13}C (14.1 T, 12.5 kHz) MAS NMR spectra of Ga-MIL-53 calcined for 96 h at 260 °C. In (a), the NMR spectrum was acquired immediately after calcination, while in (b) the sample was sealed and stored for 14 days before spectral acquisition. The spectra in (c) and (d) are for the same two samples acquired after storage (sealed from moisture) for a further 14 days.

S5. Further NMR spectra of calcined (Al,Ga)-MIL-53

Figure S5.1 shows ^{13}C CP MAS NMR spectra of calcined ($Al_{0.1}Ga_{0.9}$)-MIL-53 obtained with different CP contact times. Although the absolute signal intensity in the spectrum varies with contact time, the relative intensities of the peaks attributed to carboxylate carbons in the NP and OP forms (at δ = 175 ppm and δ = 171 ppm, respectively), does not vary, enabling the variation in the relative proportions of the two forms with the MOF composition to be determined. The values extracted from Figure 2 of the main text are given in Table S5.1. Note the absolute proportion of the two forms present in mixed metal samples cannot be determined, owing to the non quantitative nature of CP experiments, and the different distances of species to ^{1}H with the change in pore diameter.

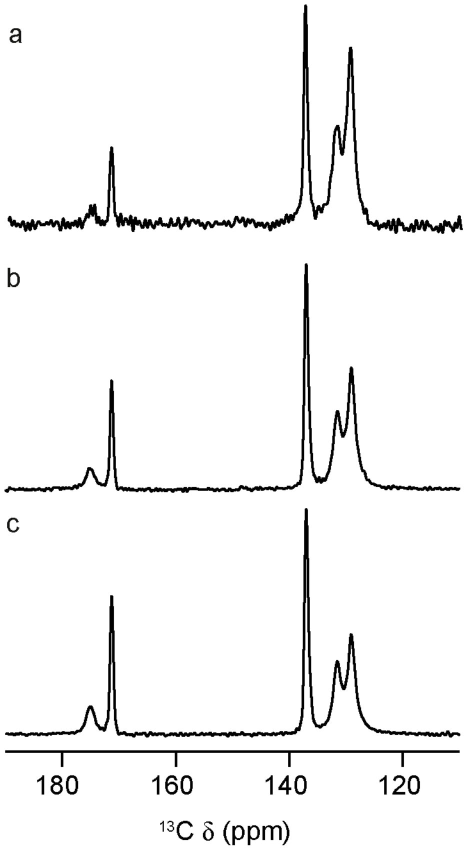

Figure S5.1. ^{13}C (14.1 T, 12.5 kHz) CP MAS NMR spectra of calcined ($Al_{0.1}Ga_{0.9}$)-MIL-53, acquired with CP contact times of (a) 1 ms, (b) 2.5 ms and (c) 5 ms.

Table S5.1. Ratio of the relative intensities of the resonances attributed to carboxylate carbons in the ^{13}C CP MAS NMR spectra shown in Figure 2 of the main text in the NP and OP forms of calcined (Al,Ga)-MIL-53, NP : OP, for varying compositions.

x	Actual composition Al : Ga	Relative ratio NP : OP forms
0.0	100 : 0	6 : 94
0.2	84 : 16	11 : 89
0.5	74 : 26	8 : 91
0.8	42 : 58	43 : 57
0.9	35 : 65	35 : 65
0.95	15 : 85	15 : 89
1.0	0 : 100	99 : 1[a]

[a] calcined at 260 °C

Figure S5.2 shows ^{1}H MAS NMR spectra of calcined ($Al_{1-x}Ga_x$)-MIL-53, confirming that the presence of the NP form does not result from exposure to water.

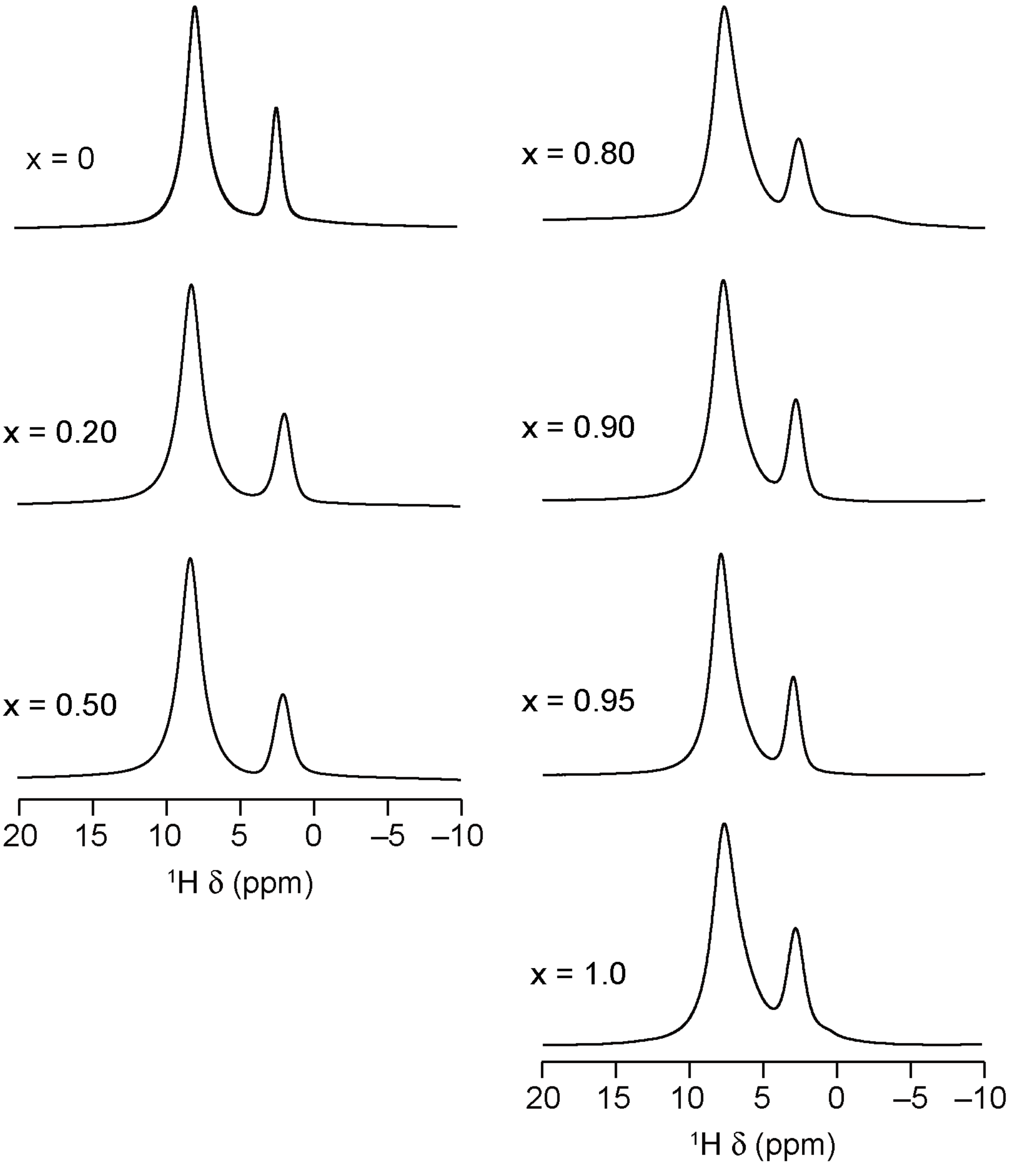

Figure S5.2. ^{1}H (14.1 T, 12.5 kHz) MAS NMR spectra of calcined ($Al_{1-x}Ga_x$)-MIL-53 for nominal compositions of x = 0, 0.2, 0.5, 0.8, 0.9, 0.95 and 1.

S6. Characterisation of calcined (Al,Ga)-MIL-53 prepared by hydrothermal synthesis

Figure S6.1 shows an ^{17}O MAS NMR spectrum (acquired using a spin echo) of calcined $Al_{0.5}$,$Ga_{0.5}$-MIL-53, synthesised hydrothermally and subsequently steamed with 130 μL of 90% $H_2{}^{17}O_{(l)}$). This shows resonances corresponding to carboxyl oxygens at ~200 ppm and hydroxyl oxygens at ~0 ppm. Fitting of the three components in the hydroxyl region (*i.e.*, Al-OH-Al, Al-OH-Ga and Ga-OH-Ga) is shown in Figure S6.2a, and is compared to that for a sample synthesised and enriched in previous work (Ref. 22 of the main text) using DGC in Figure S6.2b. Parameters from these fits are given in Table 3 of the main text. The similarity of the relative intensities of each of the three components confirm that the synthesis route does not affect the overall cation distribution in (Al,Ga)-MIL-53.

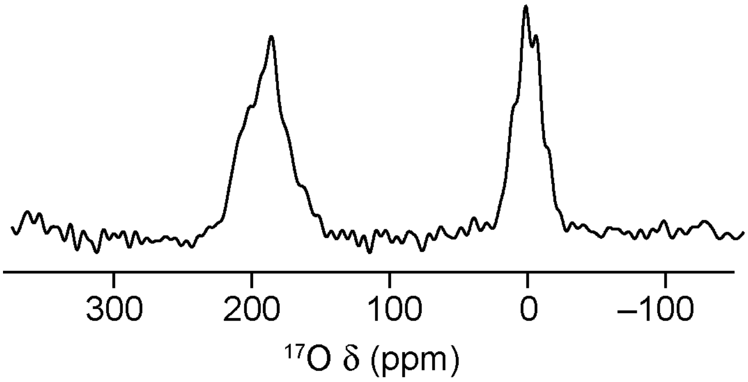

Figure S6.1. ^{17}O (20.0 T, 20 kHz) MAS NMR spectrum of calcined ($Al_{0.5}Ga_{0.5}$)-MIL-53 synthesised hydrothermally and enriched with ^{17}O *via* post-synthetic steaming.

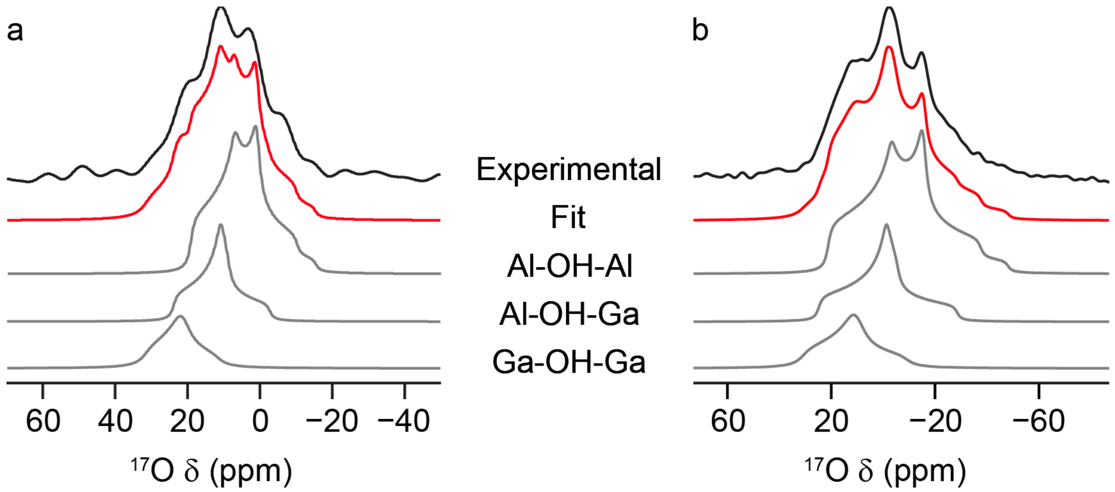

Figure S6.2. Fitting of the hydroxyl regions of (a) ^{17}O (20.0 T, 20 kHz) MAS NMR spectrum of calcined ($Al_{0.5}Ga_{0.5}$)-MIL-53 synthesised hydrothermally and enriched with ^{17}O *via* post-synthetic steaming and (b) ^{17}O (14.1 T, 20 kHz) MAS NMR spectrum of calcined ($Al_{0.5}Ga_{0.5}$)-MIL-53 synthesised and enriched using DGC (Ref. 22 of main text).

S7. Characterisation of hydrated (Al,Ga)-MIL-53

Figure S7.1a shows ^{13}C CP MAS NMR spectra of calcined, hydrated ($Al_{1-x}Ga_x$)-MIL-53, confirming all MOFs adopt the CP form upon interaction with water. Corresponding ^{1}H MAS NMR spectra are shown in Figure S7.1b, and confirm the presence of water in all samples. Figure S7.2 shows ^{17}O MAS and MQMAS NMR spectra of calcined, hydrated ($Al_{1-x}Ga_x$)-MIL-53. Regions corresponding to the carboxylate oxygens and hydroxyl oxygens are shown separately. Note, there is little resolution of signals from the chemically distinct hydroxyl oxygens at this field strength.

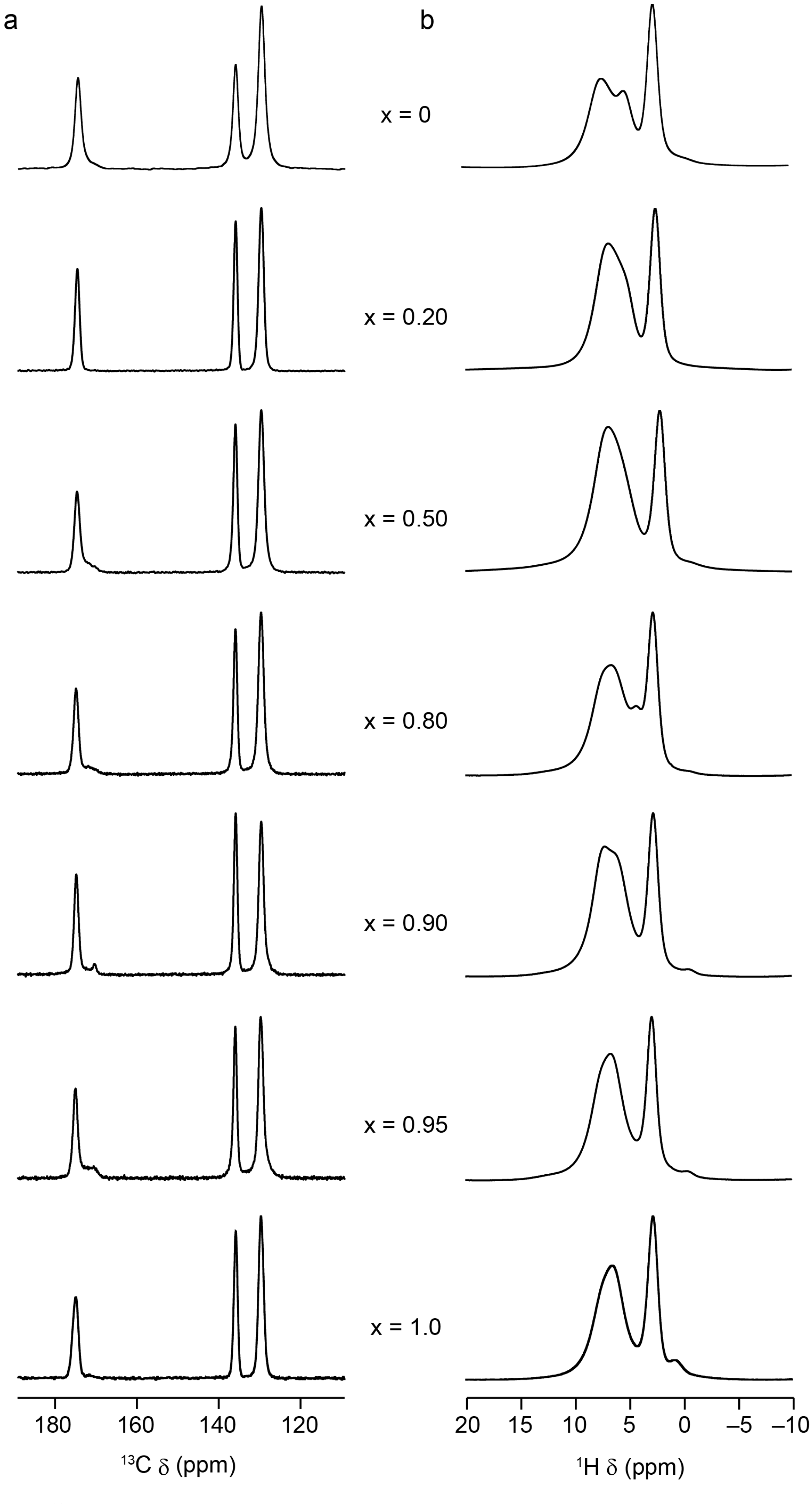

Figure S7.1. (a) ^{13}C (14.1 T, 12.5 kHz) CP MAS and (b) ^{1}H (14.1 T, 12.5 kHz) MAS NMR spectra of calcined, hydrated ($Al_{1-x}Ga_x$)-MIL-53 for nominal compositions of x = 0, 0.2, 0.5, 0.8, 0.9, 0.95 and 1.

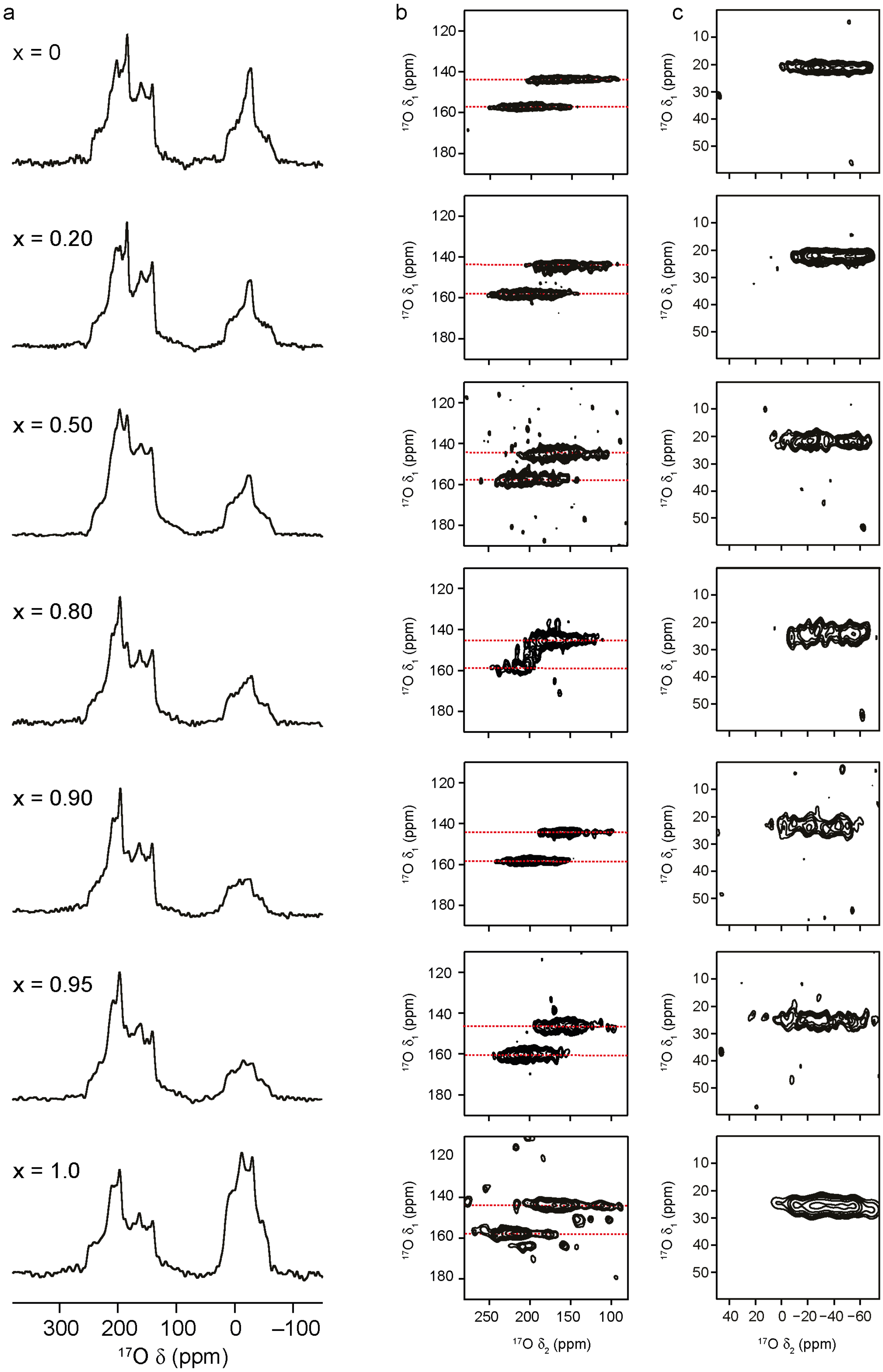

Figure S7.2. ^{17}O (14.1 T, 20 kHz) (a) MAS and (b, c) MQMAS NMR spectra of calcined, hydrated (Al$_{1-x}$Ga$_x$)-MIL-53 for nominal compositions of x = 0, 0.2, 0.5, 0.8, 0.9, 0.95 and 1.

S8. Characterisation of dehydrated (Al,Ga)-MIL-53

Figure S8.1 shows ^{17}O MAS NMR spectra of calcined, hydrated and subsequently dehydrated (Al,Ga)-MIL-53 materials. The corresponding ^{1}H MAS spectra, shown in Figure S8.2 confirm no water is present in the materials, and that the presence of the NP form of the MOF is not a result of inefficient dehydration. For completeness, Figure S8.3 shows an expansion of hydroxyl region in the ^{17}O MQMAS NMR spectra of the dehydrated (Al,Ga)-MIL-53 materials

Table S8.1 shows the variation in the relative proportions of NP and OP forms of MIL-53 determined from the ^{13}C CP MAS NMR spectra of calcined, hydrated and subsequently dehydrated (Al,Ga)-MIL-53 shown in Figure 6 of the main text. Dehydration was carried out at 120 °C. The table shows there is a systematic increase in the proportion of the NP form as the Ga content increases.

Table S8.1. Ratio of the relative intensities of the resonances attributed to carboxylate carbons in the ^{13}C CP MAS NMR spectra shown in Figure 6 of the main text in the NP and OP forms of calcined, hydrated and subsequently dehydrated (Al,Ga)-MIL-53, NP : OP, for varying compositions.

x	Actual composition Al : Ga	Relative ratio NP : OP forms
0.0	100 : 0	9 : 91
0.2	84 : 16	48 : 52
0.5	74 : 26	69 : 31
0.8	42 : 58	93 : 7
0.9	35 : 65	98 : 2
0.95	15 : 85	88 : 12
1.0		98 : 2

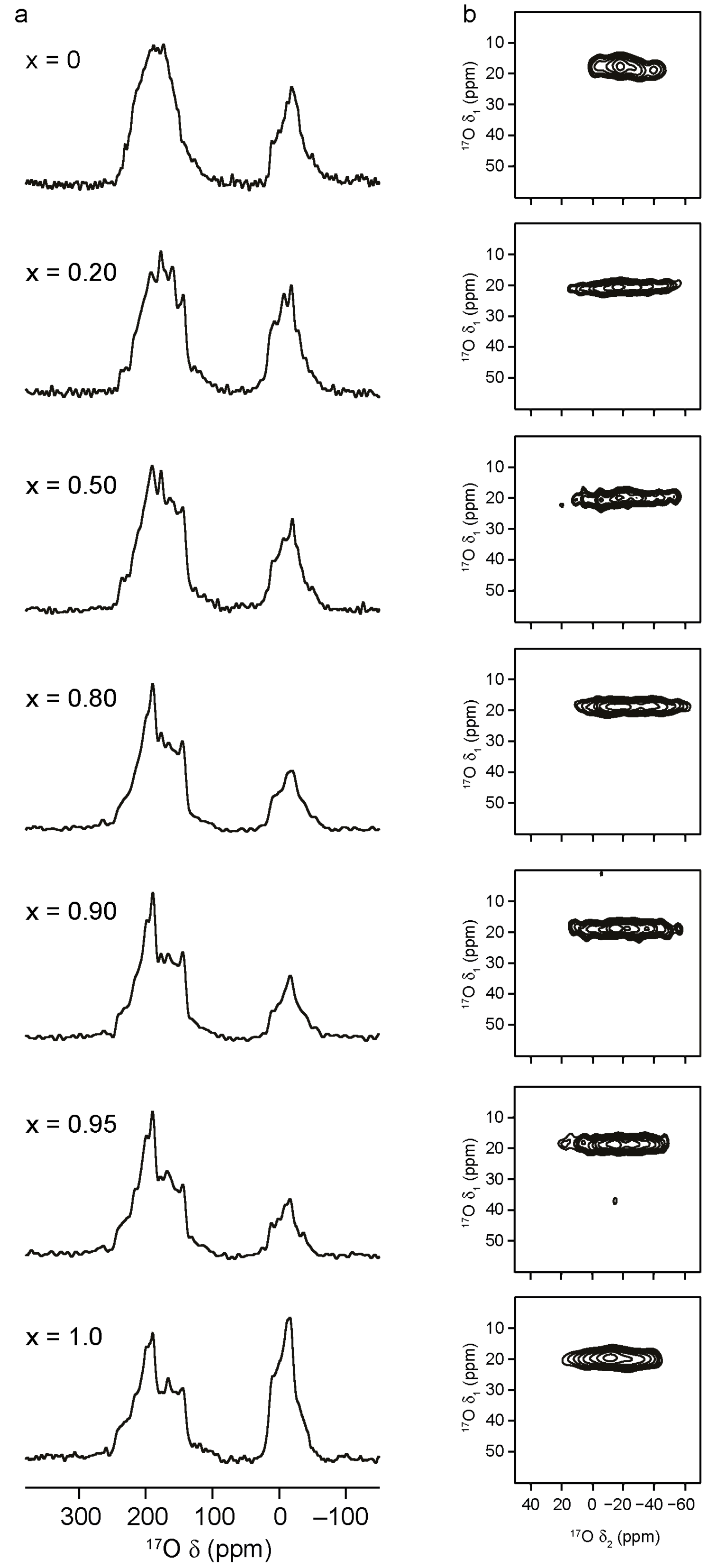

Figure S8.1 ^{17}O (14.1 T, 12.5 kHz) (a) MAS and (b) MQMAS (showing only and expansion of hydroxyl region) NMR spectra of calcined, hydrated and subsequently dehydrated ($Al_{1-x}Ga_x$)-MIL-53 for nominal compositions of x = 0, 0.2, 0.5, 0.8, 0.9, 0.95 and 1.

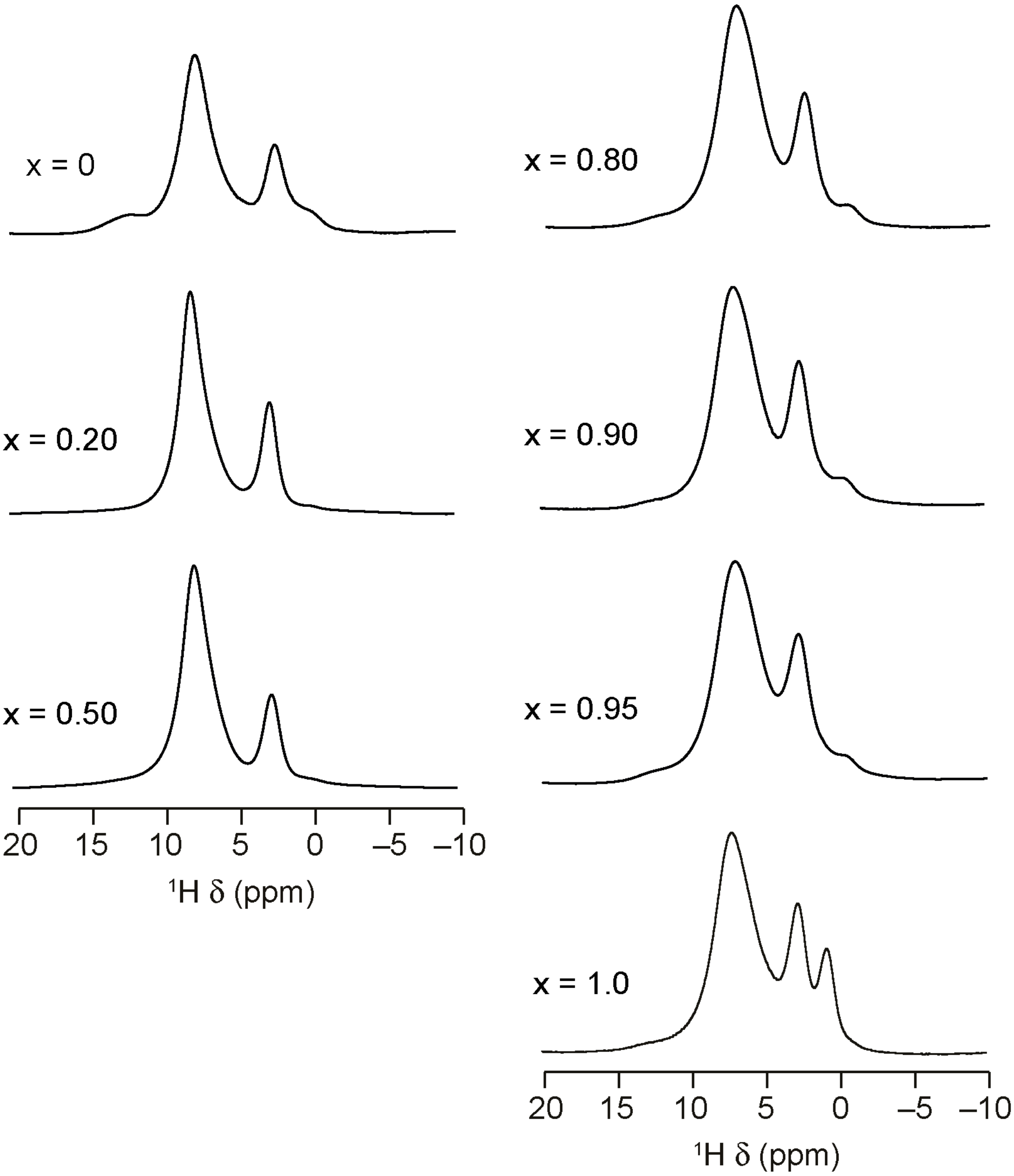

Figure S8.2 ^{1}H (14.1 T, 12.5 kHz) MAS NMR spectra of calcined, hydrated and subsequently dehydrated $(Al_{1-x}Ga_x)$-MIL-53 for nominal compositions of x = 0, 0.2, 0.5, 0.8, 0.9, 0.95 and 1.